

## Supplementary information for

### Ultraweak light-modulated heterostructure with bidirectional photoresponse for static and dynamic image perception

*Xun Han<sup>1,+</sup>, Juan Tao<sup>2,3,+</sup>, Yegang Liang<sup>3</sup>, Feng Guo<sup>1,4</sup>, Zhangsheng Xu<sup>3</sup>, Wenqiang Wu<sup>3</sup>, Jiahui Tong<sup>2</sup>, Mengxiao Chen<sup>5\*</sup>, Caofeng Pan<sup>6\*</sup>, Jianhua Hao<sup>1,4\*</sup>*

1. Department of Applied Physics, The Hong Kong Polytechnic University, Hong Kong 999077, P. R. China

2. Jiashan Fudan Institute, Jiaxing 314110, P. R. China

3. CAS Center for Excellence in Nanoscience, Beijing Key Laboratory of Micro-nano Energy and Sensor, Beijing Institute of Nanoenergy and Nanosystems, Chinese Academy of Sciences, Beijing, 101400, P. R. China

4. The Hong Kong Polytechnic University Shenzhen Research Institute, Shenzhen 518057, P. R. China

5. College of Biomedical Engineering & Instrument Science, Zhejiang University, Hangzhou 311200, P. R. China

6. Institute of Atomic Manufacturing, Beihang University, Beijing 100191, P. R. China

<sup>+</sup>These authors contributed equally

<sup>\*</sup>Correspondence and requests for materials should be addressed to M. C. (email: mengxiaochen@zju.edu.cn), to C.P. (email: pancaofeng@buaa.edu.cn), or to J. H. (email: jh.hao@polyu.edu.hk)

# Table of Contents

Supplementary Note I: Fabrication and characterization of the bidir-ZC neuromorphic image sensor array.....	3
Supplementary Note II: Yield and reproducibility of the bidir-ZC device array .....	6
Supplementary Note III: The light intensity- and bias-dependent Neg-PC and Pos-PC effect. ....	7
Supplementary Note IV: Bidirectional photoresponse in different heterojunctions with metal oxide semiconductors and metal halide perovskites. ....	12
Supplementary Note V: Synaptic behavior of the bidir-ZC device. ....	14
Supplementary Note VI: Photoresponse of the bidir-ZC device with different ZnO channel thickness. ....	17
Supplementary Note VII: The effect of $V_g$ on the negative photoresponse. ....	20
Supplementary Note VIII Denoising of the input image based on the bidir-ZC device array.....	23
Supplementary Note IX Moving object recognition demonstration based on the bidir-ZC device array.....	25

**Supplementary Note I: Fabrication and characterization of the bidir-ZC neuromorphic image sensor array.** Supplementary Fig. 1a illustrates the fabrication process of the bidir-ZC neuromorphic image sensor array. The detailed step-by-step fabrication procedures are listed below.

**a. Bottom electrode formation:**

1. Clean glass substrates sequentially with acetone, isopropanol and deionized (DI) water, then dry the substrates with nitrogen.
2. Define Au bottom electrode pattern using photolithography.
3. Deposit Au on the glass substrate via sputtering and strip photoresist.

**b. ZnO film deposition:**

4. Define ZnO pattern ( $300\ \mu\text{m} \times 300\ \mu\text{m}$  for each pixel) using photolithography, aligning with the Au electrode.
5. Deposit 60 nm ZnO film via sputtering and strip photoresist.

**c. Surface treatment for CsPbBr<sub>3</sub> array formation:**

6. Treat the ZnO surface with 10s oxygen plasma to make it hydrophilic.
7. Pattern a photoresist array ( $280\ \mu\text{m} \times 280\ \mu\text{m}$  for each pixel) on the ZnO film using photolithography.
8. Deposit 50 nm SiO<sub>2</sub> film via sputtering, covering areas outside the ZnO film and bottom electrode pad.
9. Immerse the device in octadecyl-trichlorosilane (OTS) solution (OTS:n-Hexane = 1:200) for 15 minutes to create a hydrophobic surface.
10. Remove from OTS solution and immediately place in acetone for photoresist stripping and clean with DI water.

**d. CsPbBr<sub>3</sub> film array formation in a glove box:**

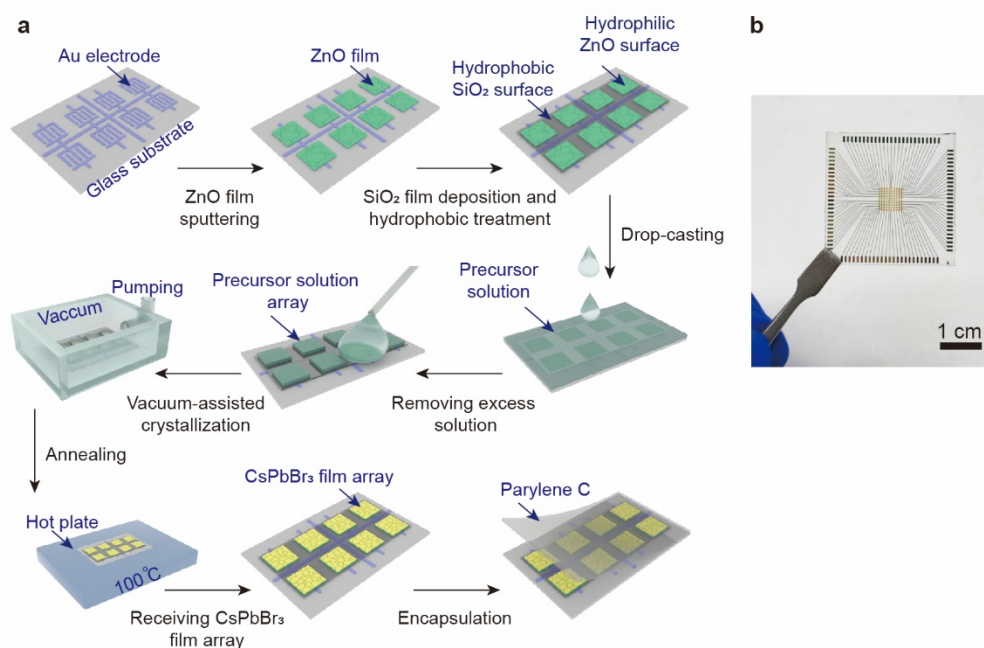
11. Prepare precursor solution (0.4 M, DMSO as solvent).
12. Drop-cast the precursor solution onto the entire device surface at room temperature, and then remove the excess solution using a pipette, allowing precursor to remain only on hydrophilic ZnO surface.
13. Place the device in a vacuum chamber at approximately 1 kPa for 30 minutes.
14. Anneal the device at 100 °C for 10 minutes to improve CsPbBr<sub>3</sub> film quality. (The

dimension and thickness of the CsPbBr<sub>3</sub> film pixel is 280  $\mu\text{m}$   $\times$  280  $\mu\text{m}$  and about 480 nm, respectively.)

#### e. Device encapsulation:

15. Deposit a 3  $\mu\text{m}$  layer of parylene-C film to enhance stability via a parylene deposition system.

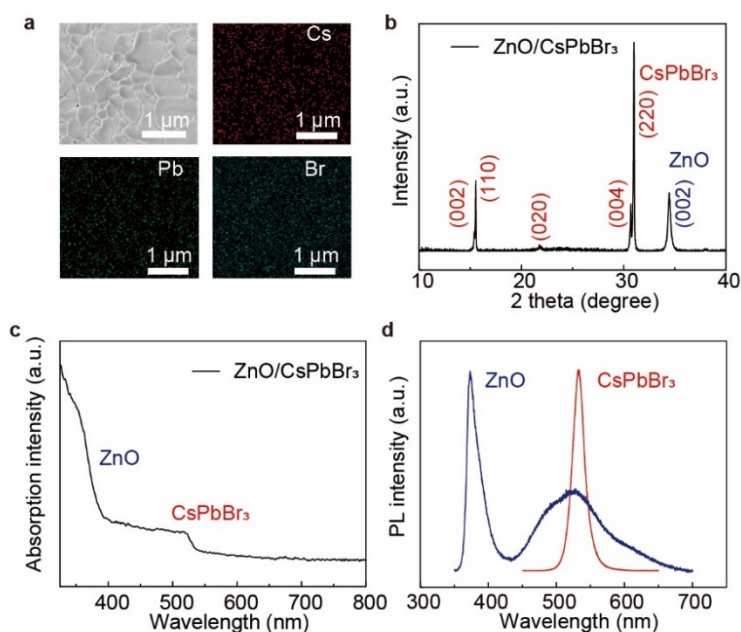
The fabrication process for devices based on ZnO/MAPbBr<sub>3</sub>, ZnO/PEA<sub>2</sub>MA<sub>3</sub>Pb<sub>4</sub>I<sub>13</sub>, and IGZO/MAPbI<sub>3</sub> heterojunctions closely resembled that of the ZnO/CsPbBr<sub>3</sub> device. Both ZnO and IGZO films were deposited using sputtering. The primary distinction lies in the formation of the perovskite films, which were created using spin-coating methods. The respective perovskites were dissolved in DMF at concentrations of 1.5 M for MAPbBr<sub>3</sub>, 1.1 M for MAPbI<sub>3</sub>, and 0.4 M for PEA<sub>2</sub>MA<sub>3</sub>Pb<sub>4</sub>I<sub>13</sub>. The active layer area is approximately 5 mm  $\times$  5 mm, with a single pixel area of 300  $\mu\text{m}$   $\times$  300  $\mu\text{m}$ , as shown in Supplementary Fig. 1b.



**Supplementary Fig. 1. Fabrication process of the bidir-ZC neuromorphic image sensor array.** **a** Schematic illustration of the fabrication process of the bidir-ZC neuromorphic image sensor array. **b** Optical image of a 10 $\times$ 10 bidir-ZC neuromorphic image sensor array.

The morphology, crystal structure, and optical properties of the ZnO/CsPbBr<sub>3</sub> heterojunction were characterized using scanning electron microscopy (SEM), X-ray

diffraction (XRD) spectroscopy, absorption spectrum, and photoluminescence spectroscopy, respectively (Supplementary Fig. 2). The CsPbBr<sub>3</sub> film exhibits a compact surface with large grains and a homogeneous distribution of elements. As shown in Supplementary Fig. 2b, the two strong diffraction peaks at 15.2° and 30.7° correspond to the (110) and (220) orthorhombic crystallographic planes of the CsPbBr<sub>3</sub> film, while the peak at 34.4° is attributed to the (002) plane of the wurtzite ZnO film. The peak splitting around the two strong peaks further confirms the orthorhombic structure of the CsPbBr<sub>3</sub> film. Supplementary Fig. 2c and Supplementary Fig. 2d illustrate the absorption spectrum and photoluminescence spectroscopy of the ZnO and CsPbBr<sub>3</sub> films.

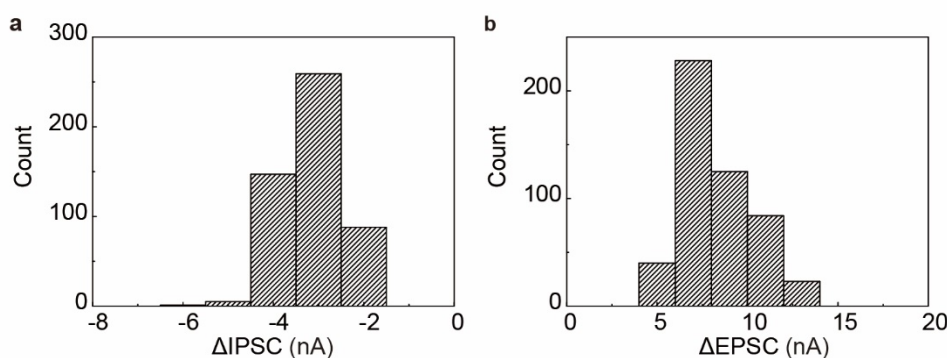


**Supplementary Fig. 2. Characterization of ZnO/CsPbBr<sub>3</sub> heterojunction.** **a** SEM image and EDS mapping of the CsPbBr<sub>3</sub> film. **b** X-ray diffraction spectrum of ZnO/CsPbBr<sub>3</sub> heterojunction. **c** Absorption spectrum of ZnO/CsPbBr<sub>3</sub> heterojunction. **d** PL spectrum of ZnO and CsPbBr<sub>3</sub> film.

## Supplementary Note II: Yield and reproducibility of the bidir-ZC device array.

The fabrication process of the bidir-ZC device array employed a combination of well-established techniques, including photolithography for precise electrode patterning and alignment, magnetron sputtering for uniform ZnO film deposition, solution-based growth of CsPbBr<sub>3</sub>, and parylene encapsulation for stability improving. Each of these techniques is industry-proven and offers excellent reproducibility. Through carefully controlling potential errors during the fabrication process, such as minimizing the mask misalignment to prevent connection between electrodes and CsPbBr<sub>3</sub>, avoiding dust contamination to prevent electrode discontinuities, ensuring consistent materials deposition, a high yield and reproducibility could be achieved.

To further validate the reproducibility and reliability of our fabrication method, we repeated the fabrication process for multiple devices. These devices exhibited a high yield of 100% and excellent reproducibility, as shown in Supplementary Fig. 3. All the 500 pixels were fully functional, demonstrating both Neg-PC and Pos-PC as expected, where the distribution of the change of inhibitory postsynaptic current ( $\Delta$ IPSC) and the change of excitatory postsynaptic current ( $\Delta$ EPSC) were tightly concentrated, indicating high consistency across pixels. Thus, our device fabrication method is both straightforward and highly reliable.

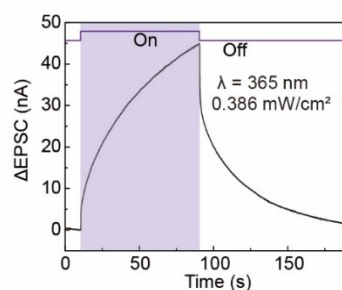


**Supplementary Fig. 3. Statistical distribution of photocurrent responses from 500 pixels across five devices.** **a** Histogram of the  $\Delta$ IPSC under 250 nW/cm<sup>2</sup> green light stimulation, demonstrating the Neg-PC effect. **b** Histogram of the  $\Delta$ EPSC under 10 mW/cm<sup>2</sup> green light stimulation, illustrating the Pos-PC effect.

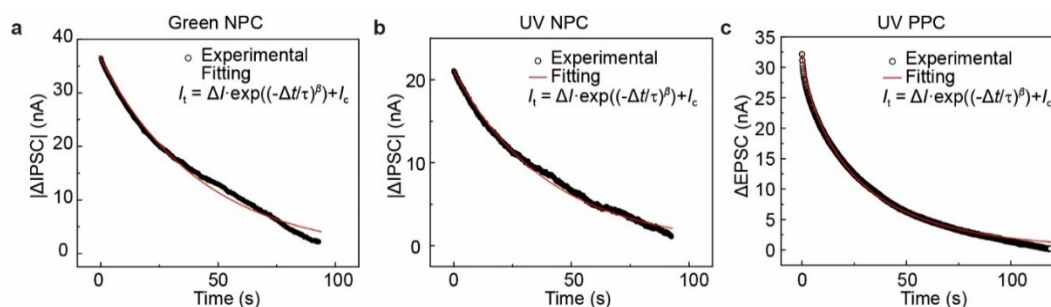
**Supplementary Note III: The light intensity- and bias-dependent Neg-PC and Pos-PC effect.** The bidir-ZC device exhibited a highly light-intensity-dependent photoresponse under both green and UV light illumination. This response was characterized by an initial enhancement followed by a depression of the Neg-PC effect, which further transitioned to the Pos-PC effect as the light intensity increased. The changes in photocurrent in the Neg-PC mode under green and UV light illumination are demonstrated in Figure 2. Supplementary Fig. 4 shows the photocurrent changes in the Pos-PC mode under continuous UV light illumination for 80 seconds with a high intensity of 0.386 mW/cm<sup>2</sup>. After removing the illumination, the postsynaptic current (PSC) gradually recovered, and the recovery process for both Neg-PC and Pos-PC modes could be fitted with a Kohlrausch stretched-exponential function<sup>1</sup> (Supplementary Fig. 5).

$$I_t = \Delta I \times \exp \left[ - \left( \frac{t}{\tau} \right)^\beta \right] + I_c \quad (1)$$

where  $\tau$  and  $\beta$  are the relaxation time and the stretching exponent, respectively.  $I_c$  is the initial current before illumination.

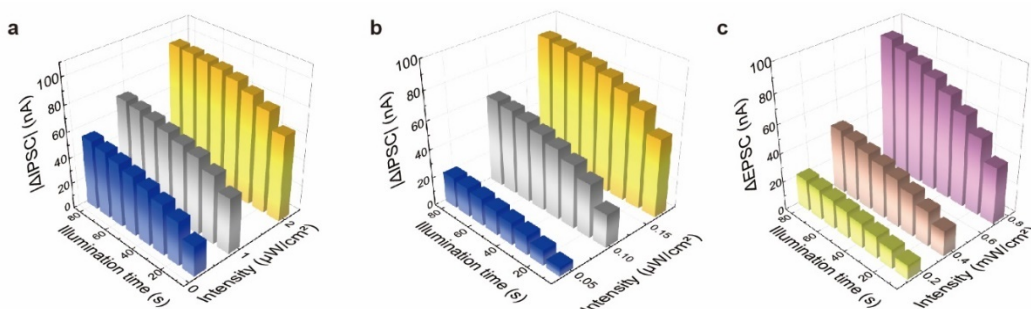


**Supplementary Fig. 4. Photocurrent change of the bidir-ZC device under UV light illumination.** Pos-PC effect was observed under the continuous UV light illumination with the intensity of 0.386 mW/cm<sup>2</sup>.



**Supplementary Fig. 5. Recovery process of the PSC.** Recovery process of the PSC. **a** Recovery process of the IPSC induced by the Neg-PC effect under green light stimulation with an intensity of 250 nW/cm<sup>2</sup>. **b** Recovery process of the IPSC induced by the Neg-PC effect under UV light stimulation with an intensity of 45 nW/cm<sup>2</sup>. **c** Decaying process of the EPSC induced by the Pos-PC effect under UV light stimulation with an intensity of 0.386 mW/cm<sup>2</sup>.

Supplementary Fig. 6 shows the PSCs of the device under continuous illumination with varying intensities. As depicted in Supplementary Fig. 6a and Supplementary Fig. 6b, the device operates in the Neg-PC mode, where either prolonged duration or high intensity results in a significant reduction in photocurrent. In contrast, under strong illumination conditions, the device exhibits the Pos-PC effect, generating a stable positive photocurrent change as both duration and intensity increase (Supplementary Fig. 6c).

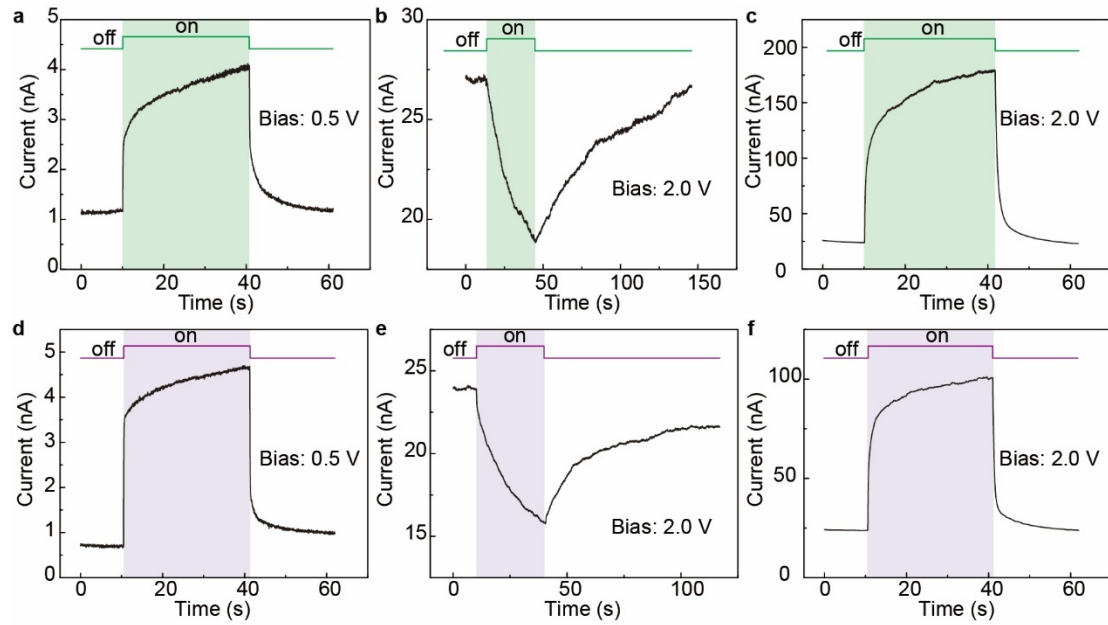


**Supplementary Fig. 6. PSC evolution process of the bidir-ZC device under green and UV light illumination with various intensities.** **a** IPSC of the device under green light stimulation in Neg-PC mode. **b** IPSC of the device under UV light stimulation in Neg-PC mode. **c** EPSC of the device under UV light stimulation in Pos-PC mode.

The bidir-ZC device also demonstrates a strong bias voltage-dependent photoresponse behavior. As shown in Supplementary Fig. 7a and Supplementary Fig. 7d, the device exhibits only the Pos-PC effect under low-intensity illumination with a small bias voltage of 0.5 V. However, when a 2.0 V bias voltage is applied, the device displays light intensity-dependent Neg-PC and Pos-PC behaviors under both green



(Supplementary Fig. 7b and Supplementary Fig. 7c) and UV light illumination (Supplementary Fig. 7e and Supplementary Fig. 7f). Additionally, the device shows a nonlinear response to the applied voltage: a 0.5 V bias results in a stable current of 1 nA, whereas a 2.0 V bias causes the current to become unstable before stabilizing at 25 nA. This phenomenon, where a fourfold increase in bias voltage results in a 25-fold increase in current, can be attributed to the capturing and releasing of carriers by the defect states and traps within the ZnO film. These defects often originate from oxygen vacancies, a type of defect that has been widely researched.



**Supplementary Fig. 7. Bias-dependent Neg-PC and Pos-PC behavior.** (a-c) Current change of the bidir-ZC device under the green light illumination with different intensity and bias. **a** Intensity is 250 nW/cm<sup>2</sup> and bias is 0.5 V. **b** Intensity is 250 nW/cm<sup>2</sup> and bias is 2.0V. **c** Intensity is 15.69 mW/cm<sup>2</sup> and bias is 2.0V. (d-f) Current change of the bidir-ZC device device under the UV light illumination with different intensity and bias. **d** Intensity is 45 nW/cm<sup>2</sup> and bias is 0.5 V. **e** Intensity is 45 nW/cm<sup>2</sup> and bias is 2.0 V. **f** Intensity is 1.71 mW/cm<sup>2</sup> and bias is 2.0 V.

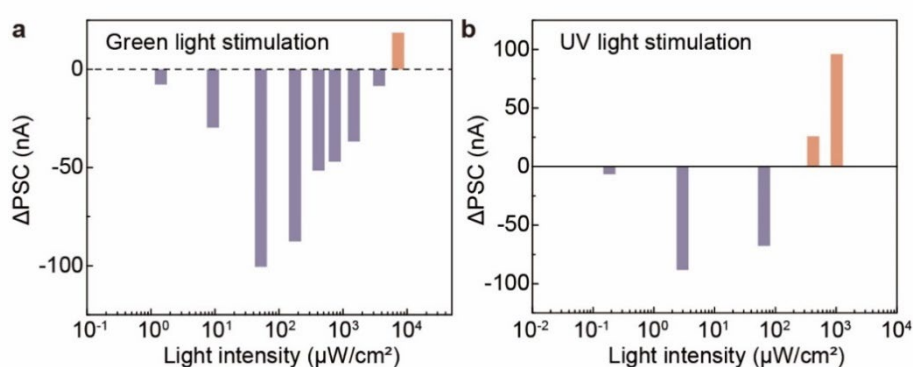
**Supplementary Table 1. Comparison of all optical modulated neuromorphic devices with bidirectional photoresponse.**

Device structure	Operation wavelength (nm)		Minimum light	Operation		Ref
	Potentialiation	Depression	intensity for Neg-PC (mW/cm <sup>2</sup> )	voltage (V)	Array	
ZnO/CsPbBr <sub>3</sub>	365, 525	365, 525	0.045×10 <sup>-3</sup> (365 nm) 0.25×10 <sup>-3</sup> (525 nm)	1.5	Y (10×10)	This work
ReS <sub>2</sub> /h-BN/MoS <sub>2</sub>	520	520	73 μW	-60, 60 (V <sub>g</sub> )	N	2
C8-BTBT/TFT-CN		365	0.005	50 (V <sub>g</sub> )	N	3
RP PVK/AlGaIn/GaN	457, 532, 660	457, 532, 660	10	-6 (V <sub>g</sub> )	N	4
DTT-8/TFT-CN	365	365	0.008	60 (V <sub>g</sub> ), 10 (V <sub>ds</sub> )	N	5
α-In <sub>2</sub> Se <sub>3</sub>	450, 520, 675	450, 520, 675	0.05	10 (V <sub>g</sub> )	N	6
Graphene/Ge	1550	1550	1.47	3 (V <sub>g</sub> )	Y (6×6)	7
IDTBT/ITO	450	450	0.096	-20 (V <sub>g</sub> )	N	8
MoS <sub>2</sub> /SiN <sub>x</sub>	405, 520, 638, 940	405, 520, 638, 940	~2μW (405 nm)	±3 - ±20 (V <sub>g</sub> )	Y (18×18)	9
WSe <sub>2</sub> /GeSe	808	808	4.1	-5	N	10
Graphene/C60/ pentacene	780, 808, 980, 1310, 1550	405, 450, 520, 650	2.43	-2 - 36 (V <sub>g</sub> )	N	11
Pyr-GDY/Gr/PbS	980	450	10	N/A	Y (7×6)	12
Graphene/C60/PbPc	980	405-850	35.4	-10 - -50 (V <sub>g</sub> )	N	13
TiO <sub>2</sub> /graphene/PbS	360	905	7.17	N/A	N	14
Modified silk fibroin protein	405	405	10 mW	0.1 (read voltage)	Y (12×12)	15

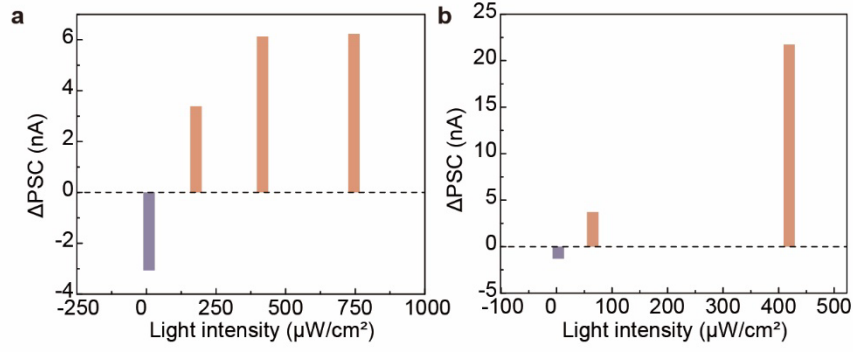
NiO/TiO <sub>2</sub>	480	320	4.48	0.1 (read voltage)	Y (8×8)	16
BP	280	365	4	0.05	N	17
InP QDs/InSnZnO	550	550	0.27	3 (V <sub>g</sub> )	Y (4×4)	18
MoS <sub>2</sub>	454	980, 1550	0.01	20 (V <sub>g</sub> )	N	19
PtSe <sub>2-x</sub>	980	405	39.09	1	N	20

---

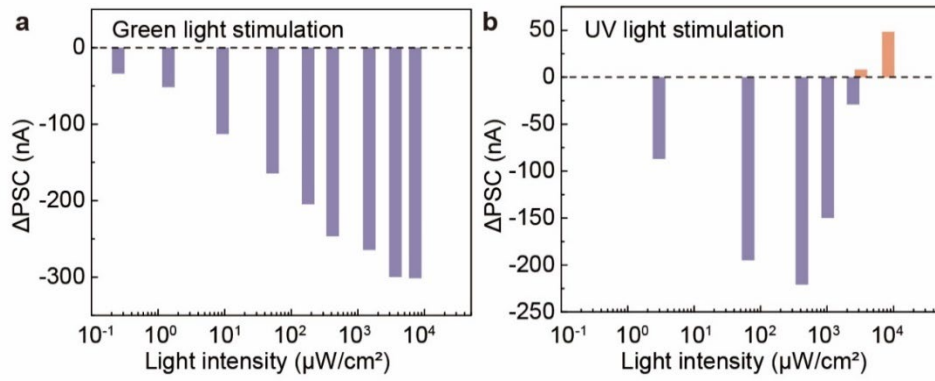
**Supplementary Note IV: Bidirectional photoresponse in different heterojunctions with metal oxide semiconductors and metal halide perovskites.** The bidirectional photoresponse behavior was also observed in other heterojunctions built with different metal oxide semiconductors and perovskites. As shown in Supplementary Fig. 8, Supplementary Fig. 9 and Supplementary Fig. 10, the devices based on the ZnO/MAPbBr<sub>3</sub>, ZnO/PEA<sub>2</sub>MA<sub>3</sub>Pb<sub>4</sub>I<sub>13</sub> and IGZO/MAPbI<sub>3</sub> heterojunctions exhibit the three stages of photocurrent change including the Neg-PC enhancement, Neg-PC suppression and Neg-PC to Pos-PC transformation with increasing intensity under both green and UV light illumination. Due to the different photoresponse performance of these active materials, the devices possess different current level and operation intensity ranges for the three stages. For example, the ZnO/MAPbBr<sub>3</sub> demonstrated clearly Neg-PC to Pos-PC transformation behavior while the IGZO/MAPbI<sub>3</sub> did not show the Pos-PC even under a high intensity of 10 mW/cm<sup>2</sup> with green stimulation. The minimum intensity required to induce the Neg-PC was also varied among these devices. What these heterojunctions have in common is that they are all type II heterojunctions, where electrons will ideally transport from the perovskite to the metal oxide semiconductor, and the conductivity of the metal oxide semiconductor is commonly related to oxygen vacancies. The specific mechanism was explained in the working mechanism section.



**Supplementary Fig. 8. Bidirectional photoresponse of ZnO/MAPbBr<sub>3</sub>-based device. a** Intensity-dependent photocurrent under green light illumination. **b** Intensity-dependent photocurrent under UV light illumination.



**Supplementary Fig. 9. Bidirectional photoresponse of ZnO/PEA<sub>2</sub>MA<sub>3</sub>Pb<sub>4</sub>I<sub>13</sub>-based device.** **a** Intensity-dependent photocurrent under green light illumination. **b** Intensity-dependent photocurrent under UV light illumination.



**Supplementary Fig. 10. Bidirectional photoresponse of IGZO/MAPbI<sub>3</sub>-based device.** **a** Intensity-dependent photocurrent under green light illumination. **b** Intensity-dependent photocurrent under UV light illumination.

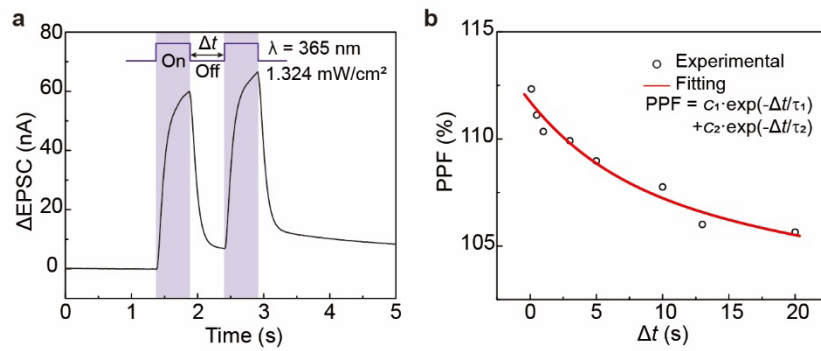
**Supplementary Note V: Synaptic behavior of the bidir-ZC device.** The synaptic behavior of the device was characterized by applying consecutive light pulses. Firstly, paired-pulse facilitation (PPF), a critical short-term plasticity behavior in neuronal networks, was implemented by applying paired pulses with various time intervals ( $\Delta t$ ). PPF refers to the phenomenon where the second spike elicits an enhanced postsynaptic current, with the degree of enhancement depending on the interval between the two spikes. This is essential for temporary information recognition and decoding. The PSC changes induced by the green and UV light in the Neg-PC mode, and by the UV light in the Pos-PC mode, are shown in Fig. 2e and Supplementary Fig. 11a. The PPF index was calculated by the ratio of the PSC change evoked by the second light pulse to that induced by the first light pulse. For both Pos-PC and Neg-PC modes, the PPF index decreased monotonically with increasing  $\Delta t$  (Fig. 2f and Supplementary Fig. 11b). The relationship between them could be fitted with the following double-exponential equation<sup>21</sup>

$$PPF = c_1 \times \exp\left(-\frac{\Delta t}{\tau_1}\right) + c_2 \times \exp\left(\frac{\Delta t}{\tau_2}\right) \quad (2)$$

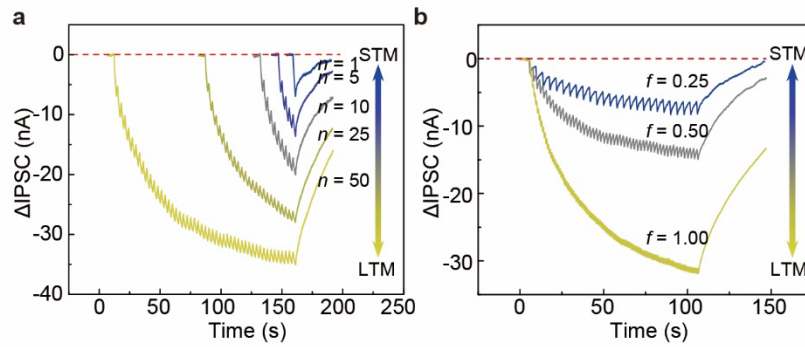
where  $\tau_1$  and  $\tau_2$  represent the characteristic relaxation time of the rapid and slow decay process. In biological neural systems, short-term memory (STM) typically refers to transient changes in synaptic strength that decay over time, whereas long-term memory (LTM) refers to more permanent changes retained over extended periods. The transition from STM to LTM can be achieved by applying repeated training and rehearsal. We mimicked this transition process by introducing light pulses with different pulse numbers and frequencies. Supplementary Fig. 12 and Supplementary Fig. 13 exhibit the IPSC change induced by green and UV light pulses in the Neg-PC mode. Increasing either the pulse numbers or frequencies led to significant photocurrent variations, resulting in smaller current values. These trapped carriers could not be released immediately after removing the light stimulus, leading to a slow change in the channel conductivity. This, in turn, facilitates the transition from STM to LTM, allowing the device to learn and retain information in a manner similar to biological systems.

The energy consumption per light pulse was calculated by the equation:  $E = I_{\text{peak}} \times t \times$

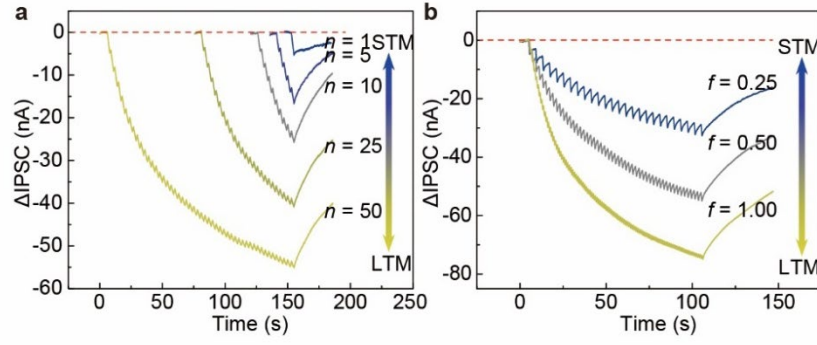
$V$ , where  $I_{\text{peak}}$  is the maximum PSC generated in each light pulse,  $t$  is the pulse width, and  $V$  is the applied voltage on the device<sup>22</sup>. As shown in Supplementary Fig. 14a, the current at the onset of each light pulse was adopted as the  $I_{\text{peak}}$  for calculating energy consumption. Due to the negative photoresponse of the device, the energy consumption per light pulse was decreased with increasing pulse numbers (Supplementary Fig. 14 b). For example, the energy consumed per light pulse reduced significantly to about 0.96 nJ by the 200th UV light pulse.



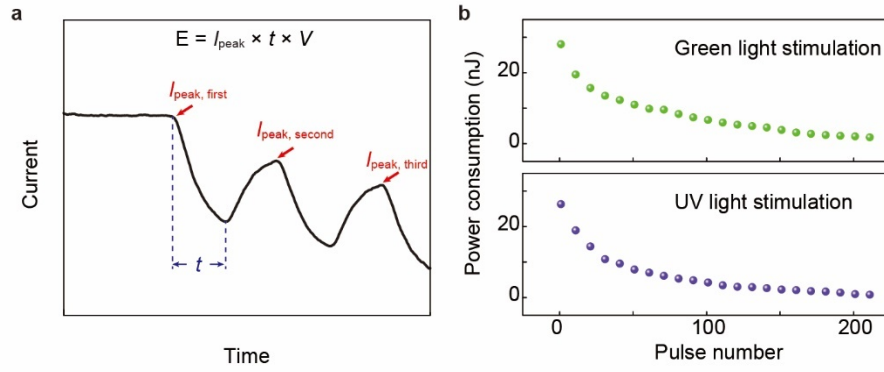
**Supplementary Fig. 11. PPF of the bidir-ZC device in Pos-PC mode. a** EPSCs of the bidir-ZC device induced by a paired UV light pulse. **b** PPF index as a function of the time interval.



**Supplementary Fig. 12. STM and LTM induced by the green light pulses in the Neg-PC mode. a, b** Transition from STM to LTM induced by increased number (a) and frequency (b) of light pulses with an intensity of 250 nW/cm<sup>2</sup>.



**Supplementary Fig. 13. STIM and LTM induced by the UV light pulses in the Neg-PC mode. a, b** Transition from STIM to LTM induced by increased number (a) and frequency (b) of light pulses with an intensity of  $45 \text{ nW/cm}^2$ .



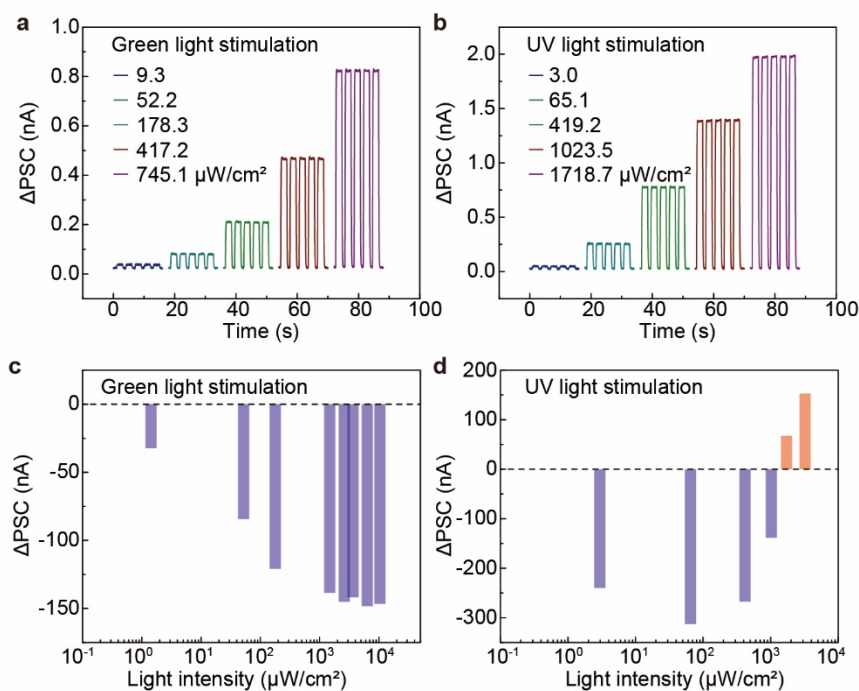
**Supplementary Fig. 14. Calculation of energy consumption of the bidir-ZC device. a** Schematic illustration of the  $I_{\text{peak}}$  for each light pulse event. **b** Energy consumption dependent on the number of pulses for each light pulse event under green ( $250 \text{ nW/cm}^2$ ) and UV ( $45 \text{ nW/cm}^2$ ) light stimulation.



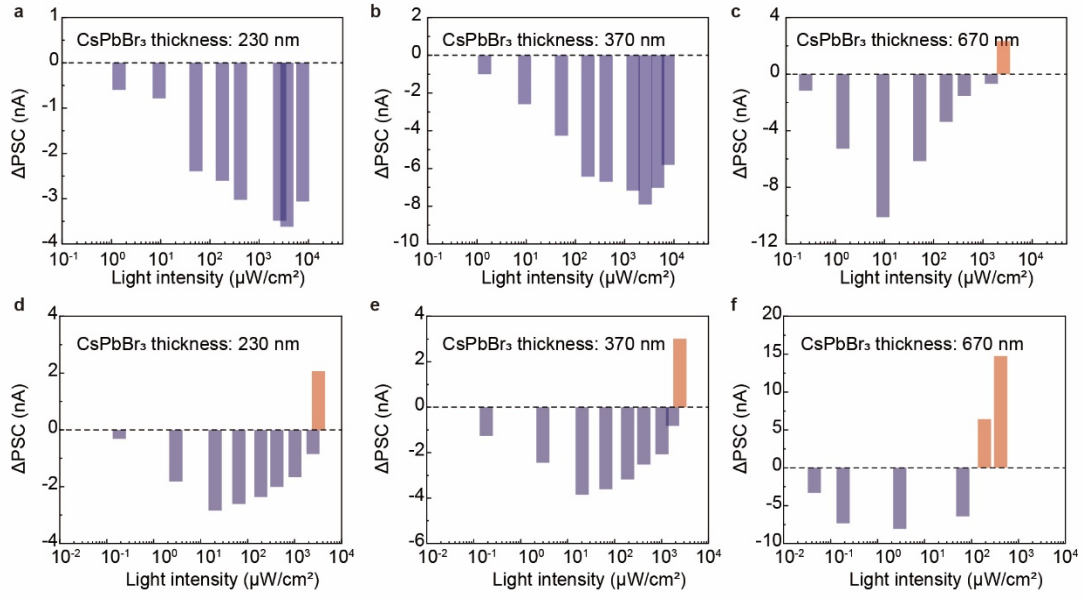
**Supplementary Note VI: Photoresponse of the bidir-ZC device with different ZnO channel and CsPbBr<sub>3</sub> film thicknesses.** Oxygen vacancies play a significant role in determining the electrical and optoelectronic properties of ZnO-based devices. The thickness of ZnO films can indeed influence the amount and distribution of oxygen vacancies within the material. The oxygen vacancies related bidirectional photoresponse is further confirmed by the ZnO and CsPbBr<sub>3</sub> thickness-dependent photobehavior.

As shown in Supplementary Fig. 15a and 15b, the device with small thickness of 30 nm demonstrates only Pos-PC effect under both green and UV light stimulation. In addition, fast photoswitching behavior was observed without persist photoconductivity caused by the oxygen vacancies. This could be because the thin ZnO film has relatively few oxygen vacancies, and when electrons transfer from the perovskite to the ZnO channel, they are mostly trapped by the oxygen vacancies. Therefore, it has low density of trap states, resulting in this fast photoswitching behavior. As a contrast, the device with a 90 nm-thick ZnO film demonstrates both Neg-PC and Pos-PC effect (Supplementary Fig. 15c and 15d). Under green light illumination, we observed only the Neg-PC behavior, even when the intensity increased to 10 mW/cm<sup>2</sup> and an enhanced intensity was required for transformation between Neg-PC and Pos-PC under UV light stimulation. Supplementary Fig. 16 demonstrated the effect of the CsPbBr<sub>3</sub> film thickness. The Neg-PC effect was observed in devices across all CsPbBr<sub>3</sub> film thickness tested and all devices exhibited the similar process that the Neg-PC effect initially intensified and then weakened as light intensity increased. However, the magnitude of this effect varied significantly. Thinner CsPbBr<sub>3</sub> layers resulted in reduced Neg-PC effects, showing lower IPCS values and decreased sensitivity to ultraweak light. Additionally, the light intensity threshold for transitioning from Neg-PC to Pos-PC decreased with increasing CsPbBr<sub>3</sub> thickness. For example, under UV light stimulation, devices with 230 nm-thick CsPbBr<sub>3</sub> film required light intensities greater than 1 mW/cm<sup>2</sup> to achieve Pos-PC, while 670 nm-thick devices needed approximately one order of magnitude lower intensity. Under green light stimulation, devices with thinner CsPbBr<sub>3</sub> layers (230 nm and 370 nm) were hard to achieve Pos-PC effect.

These phenomena could be attributed to the matching of oxygen vacancies and photogenerated carriers between ZnO and CsPbBr<sub>3</sub>. Generally, the thick ZnO film contains a large number of oxygen vacancies, which can trap a significant amount of photogenerated electrons, and the thickness of the CsPbBr<sub>3</sub> is positively correlated with the number of photogenerated carriers. As a result, devices with either a thick ZnO film or a thin CsPbBr<sub>3</sub> layer required higher light intensities to generate sufficient electrons to achieve the Pos-PC effect.



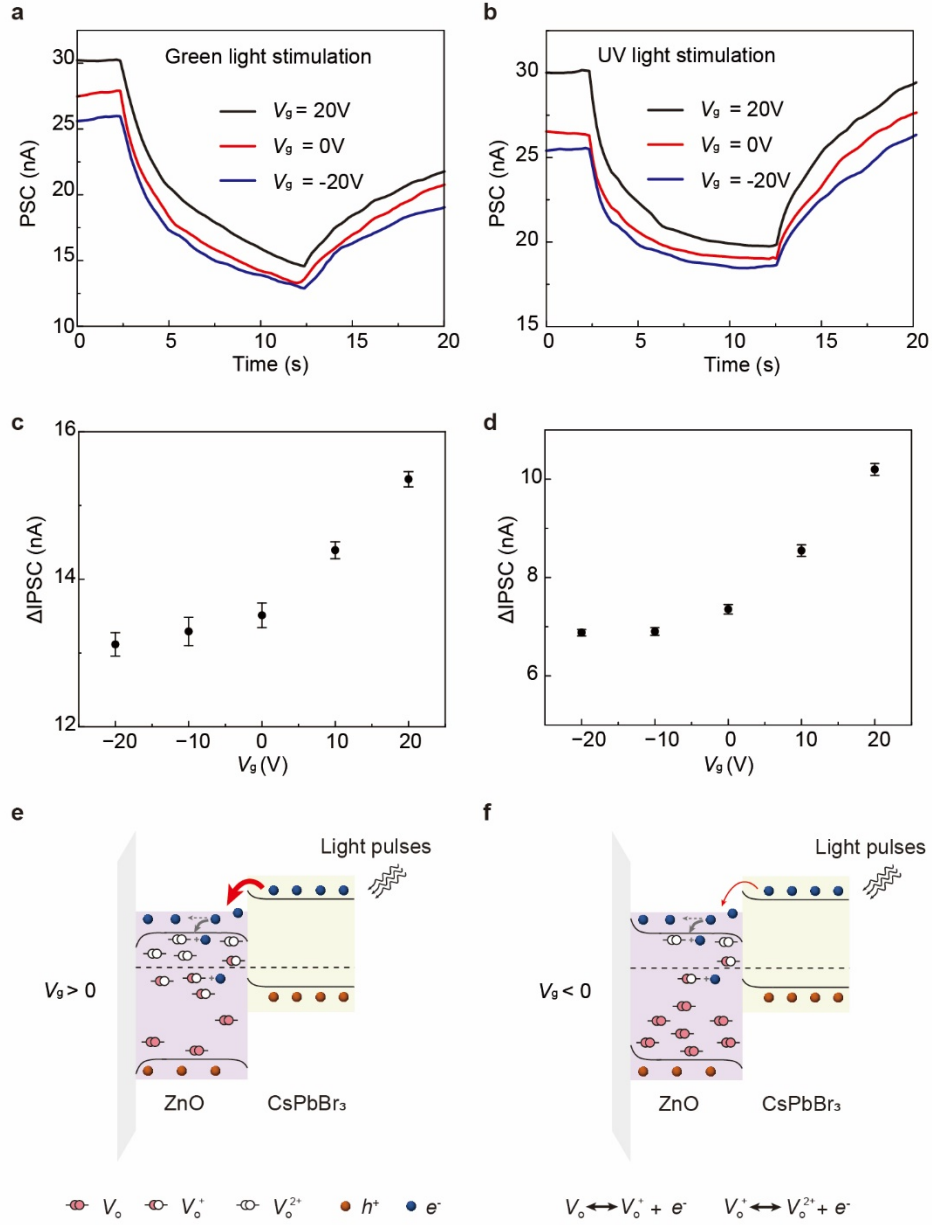
**Supplementary Fig. 15. Photocurrent of the bidir-ZC device with different ZnO thicknesses.** **a, b** Intensity-dependent photocurrent under green (a) and UV (b) light illumination with ZnO thickness of 30 nm, showing only the Pos-PC behavior. **c, d** Intensity-dependent photocurrent under green (c) and UV (d) light illumination with ZnO thickness of 90 nm, showing both Neg-PC and Pos-PC behavior. The CsPbBr<sub>3</sub> thickness for these devices remained unchanged at about 480 nm.



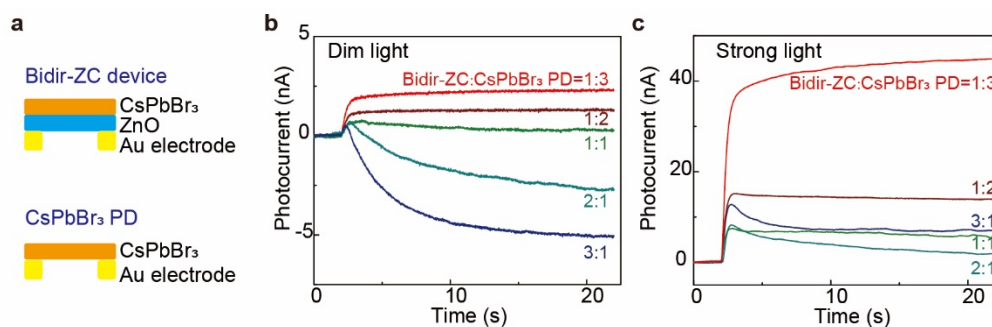
**Supplementary Fig. 16. Photocurrent of the bidir-ZC device with different CsPbBr<sub>3</sub> thicknesses.** **a-c**, Intensity-dependent photocurrent of the bidir-ZC devices under green light stimulation with CsPbBr<sub>3</sub> thickness of 230 nm, 370nm and 670 nm, respectively. **d-f**, Intensity-dependent photocurrent of the bidir-ZC devices under UV light stimulation with CsPbBr<sub>3</sub> thickness of 230 nm, 370nm and 670 nm, respectively. The ZnO thickness for these devices remained unchanged at about 60 nm.

**Supplementary Note VII: The effect of  $V_g$  on the negative photoresponse.** The bidirectional ZC device was fabricated on a silicon wafer with 300 nm-thick  $\text{SiO}_2$  layer to investigate the effect of the gate voltage ( $V_g$ ). All the device properties, such as the ZnO and  $\text{CsPbBr}_3$  thickness and pixel dimensions, were identical to those of the device on the glass substrate. The  $V_g$  from -20V to 20V was applied on the device. As shown in Supplementary Fig. 17a and 17b, as the  $V_g$  transitioned from negative to positive values, the dark current of the device gradually increased, rising from approximately 25 nA at -20V to 30 nA at 20V. This demonstrated the effect of  $V_g$  on the regulation of the ZnO channel, which may be due to the gate voltage altering the ionization states of oxygen vacancies in the ZnO channel.

Under both green light (250 nW/cm<sup>2</sup>) and UV light (45 nW/cm<sup>2</sup>) stimulation, the device exhibited clear Neg-PC behaviors under different  $V_g$ , though the value of  $\Delta\text{IPSC}$  varies. We summarized the impact of different  $V_g$  on the  $\Delta\text{IPSC}$ . As shown in Supplementary Fig. 17c and 17d,  $\Delta\text{IPSC}$  increased with increasing gate voltage. However, in the positive gate voltage range,  $\Delta\text{IPSC}$  changed significantly with increasing positive  $V_g$ , whereas in the negative gate voltage range,  $\Delta\text{IPSC}$  changed only slightly with increasing negative  $V_g$ . These results indicated the modulation effect of gate voltage on charge transfer at the interface. As shown in Supplementary Fig. 17e, positive gate voltage promoted the transfer of electrons from  $\text{CsPbBr}_3$  to the ZnO channel, leading to a greater change in  $\Delta\text{IPSC}$ . Conversely, negative gate voltage suppressed this electron transfer process, resulting in a reduced  $\Delta\text{IPSC}$  (Supplementary Fig. 17f).



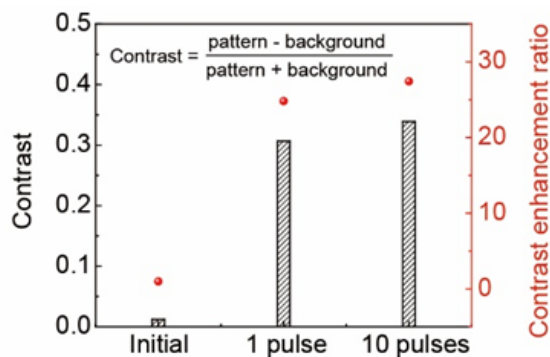
**Supplementary Fig. 17. The effect of  $V_g$  on the bidir-ZC device to achieve negative photoresponse.** Current of the bidir-ZC device under green light stimulation (**a**) and UV light stimulation (**b**) with different  $V_g$ . Gate voltage dependent-IPSC under green light stimulation (**c**) and UV light stimulation (**d**). Schematic illustration of the effect of positive  $V_g$  (**e**) and negative  $V_g$  (**f**) on the bidir-ZC device.



**Supplementary Fig. 18. Photocurrent of the combination of the bidir-ZC devices and CsPbBr<sub>3</sub> PDs with different ratios under green light illumination.** **a** The cross-sectional schematic illustrations of the bidir-ZC device and CsPbBr<sub>3</sub> PD. **b** Photocurrent under dim light illumination with intensity of 1.42  $\mu\text{W}/\text{cm}^2$ . **c** Photocurrent under strong light illumination with intensity of 1.31  $\text{mW}/\text{cm}^2$ . The bidir-ZC device demonstrated negative photoresponse in both dim and strong illumination conditions. The CsPbBr<sub>3</sub> PDs demonstrated positive photoresponse under the green light stimulation.

**Supplementary Note VIII Denoising of the input image based on the bidir-ZC device array.** The noisy image (10×10) contained both pattern and background pixels, each exhibiting different light intensities of UV light illumination, as shown in Fig. 5b. To distinguish between the pattern pixels and background pixels, the intensities of the pattern pixels were higher than those of the background pixels. This mimics how we perceive patterns in the real world, which identifies them based on color or intensity differences from the surrounding environment. The noisy image was then applied to the device arrays (10×10 pixels) using 10 UV light pulses, with each device pixel corresponding to the intensity of a pixel in the noisy image shown in Fig. 5b. Due to the Neg-PC to Pos-PC transformation property of the device as light intensity increasing, the currents of the device pixels stimulated by the pattern pixel in the noisy image were enhanced by the Pos-PC effect. Conversely, the currents of the device pixels illuminated by the background pixel of the noisy image were suppressed by the Neg-PC effect, resulting in background noise reduction.

Image contrast is a measure of the difference in luminance or color that makes an object distinguishable from other objects and the background. Here, we modified the Michelson contrast by using the difference between the average photocurrent of the pattern pixels and the background pixels to divide the sum of their average photocurrents to calculate the contrast. As shown in Supplementary Fig. 19, the image contrast was enhanced with the applied light pulses. After 10 light pulses, the image contrast increased to above 0.33, resulting in a clearly observable pattern.

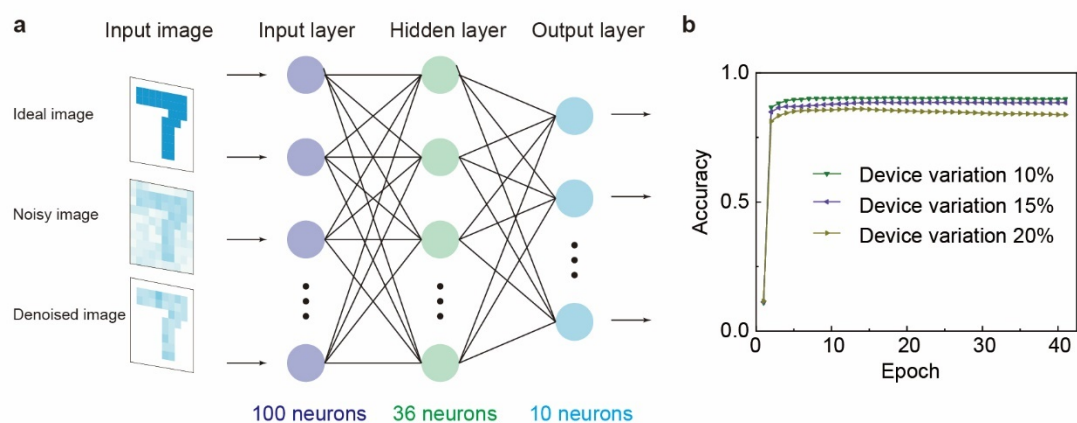


**Supplementary Fig. 19. Contrast enhancement with the light pulses.** The image contrast was calculated by taking the difference between the average photocurrent of

the pattern pixels and the background pixels, divided by the sum of their average photocurrents.

To verify the capability of our device in reducing noise in images, we built an artificial neural network consisting of an input layer, a hidden layer, and an output layer. The input layer comprised 100 neurons to accommodate the 100 pixels of each image. The hidden layer contained 36 neurons, while the output layer had 10 neurons (Supplementary Fig. 20a). The code was written in Python and executed in the integrated development environment Spyder. For the comparison, images from the standard MNIST handwritten digital image dataset were resized to 10×10 pixels to serve as ideal images, and random noise was added to create noisy images.

One challenging issue is the uniform photoresponse of pixels in array devices. For our device, this means that the transformation threshold from Neg-PC to Pos-PC for each pixel point is inconsistent. Consequently, some background pixels will be enhanced by Pos-PC, while some pattern pixels will be suppressed. Supplementary Fig. 20b shows the recognition accuracy under different device variations, showing that even with a 20% variation, the accuracy still exceeds 84%.

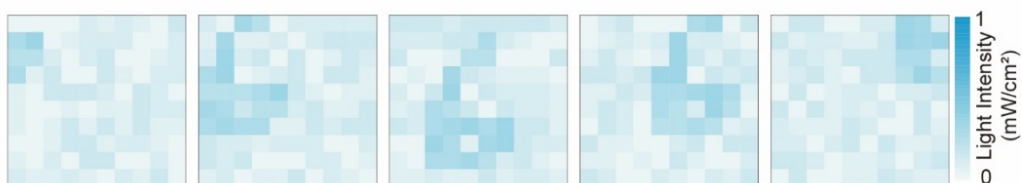


**Supplementary Fig. 20. An artificial neural network for the image recognition task.**

**ANN.** **a** Three types of images including the ideal binary images, noisy images and denoised images by the device were fed into the network for the image recognition. **b** Image recognition accuracy with different device variations.



**Supplementary Note IX Moving object recognition demonstration based on the bidir-ZC device array.** The capability of encoding the spatiotemporal information is critical for high-efficient moving perception in the machine vision systems. Due to the array configuration and the time-dependent synaptic photoresponse behavior, our device could be used to process the spatiotemporal information. To demonstrate this capability, five frames of a moving object, combined as a dynamic image, was applied onto the device array, as shown in Supplementary Fig. 21. These five frames could be considered as photographs taken by a conventional camera of a moving object. In these frames, the position of the object was constantly changing, and so was the background noise. Each pixel in these five frames would be programmed into an UV light pulse sequence, with the light intensity corresponding to the pixel value. The time of each light pulse would be set according to the time point of each frame and then applied to the pixels of the device one by one (Fig. 5f). In this way, real-time noise reduction could be achieved with each frame applied. By recording the photocurrent values after each frame was applied, a clear image of the object's motion trajectory could be obtained (Fig. 5g and Fig. 5h).



**Supplementary Fig. 21. Noisy input images of a moving object.** These five frames recorded the position of a moving object at each moment. If they are combined as a dynamic image, it would show the process of the object moving from the upper left corner to the center and then to the upper right corner.

Unsupervised approaches were useful and popular due to their simplicity without depending on training samples and labels, whereas some supervised approaches such as convolutional neural network (CNN) and fully convolution networks (FCN) relied on numerous training samples and label images via feature learning. In unsupervised algorithms, clustering represents one kind of important and popular algorithms for

grayscale and color image segmentation due to its suitable and useful for both low- and high-dimensional data<sup>23, 24</sup>. Due to the device's ability to encode spatiotemporal information while performing noise reduction, a simple unsupervised algorithm can be used to distinguish the direction of motion, which was built with PyCharm. The resulting motion images by the device were fed into an unsupervised learning algorithm for the moving perception task. As a comparison, we also fed both the ideal image and the noisy image into the network for recognition. The ideal image refers to the spatiotemporal information of a moving object being recorded by a noise-free binary image, which is then fused and compressed into a single image. In contrast, the noisy image refers to the spatiotemporal information being recorded along with background noise. Conventional image sensors tend to capture this image with background noise.

The initial task is to extract the edge contour of the main motion objects in the dynamic images to let the machine know what objects are. Fuzzy C-Means (FCM) algorithm was adopted to achieve object recognition by minimizing an objective function<sup>25</sup>. Basically, the objective function is the pairwise difference between data points and cluster centers<sup>26</sup>.

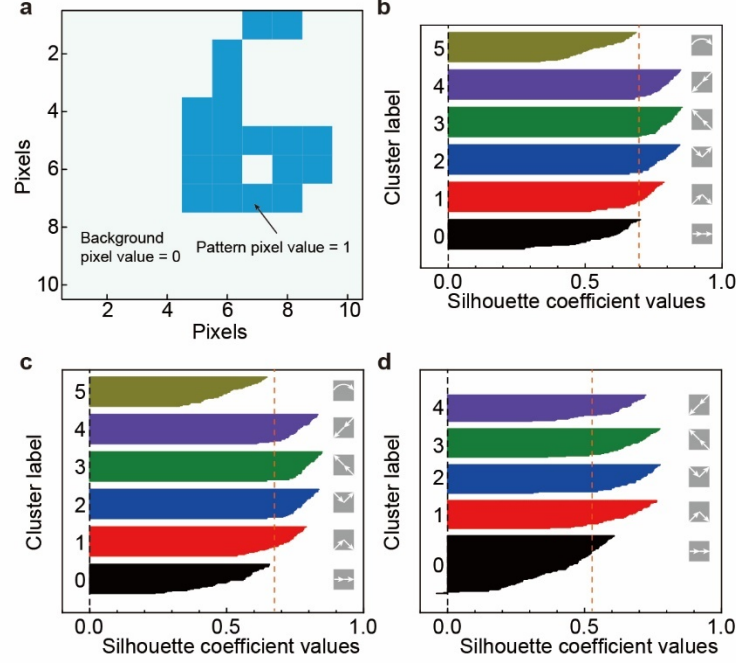
$$J = \sum_{j=1}^n \sum_{i=1}^c u_{ij}^m \|x_j - v_i\|^2 \quad (3)$$

Where  $n$  is the number of data points,  $c$  is the number of clusters,  $v_i$  is the  $i$ th cluster center,  $x_j$  is the  $j$ th data point,  $u_{ij}$  is the membership grade of the  $j$ th data point in the  $i$ th cluster (element of partition matrix  $U(c \times n)$ ),  $m$  ( $m > 1$ ) is the degree of fuzziness. Minimizing the  $J$  value of Eq (3) under the constraint condition  $\sum_{k=1}^c u_{kj} = 1$  to get the most compact clusters placed in dense regions of data.

$$v_i = \frac{\sum_{j=1}^n u_{ij}^m x_j}{\sum_{j=1}^n u_{ij}^m}, u_{ij} = \left[ \sum_{k=1}^c \left( \frac{\|x_j - v_i\|^2}{\|x_j - v_k\|^2} \right)^{\frac{1}{m-1}} \right]^{-1} \quad (4)$$

Then, the FCM algorithm begins with a random partition matrix  $U = \text{rand}(c, n)$  to initialize the algorithm. Then, the cluster centers  $v_i$  and membership degrees  $u_{ij}$  are updated by using Eq (4) until reach the algorithm convergence condition. For our device, the  $n$  is the total pixels of 100, the  $c$  is 2 based on the contour extraction, and the hyper-

parameter  $m$  is 3. After about 8 iterations, the margin of the number “6” in matrix of  $10 \times 10$  pixels can be well extracted since the algorithm convergence (Supplementary Fig. 22a).



**Supplementary Fig. 22. Moving object extraction and motion clustering using unsupervised learning method. a** Pattern "6" extracted from Fig. 5g. **b-c** SCVs of each motion recorded by the ideal (b), denoised (c) and noisy images (d). The SCV ranges from -1 to 1. A higher SCV indicates better clustering, characterized by dense and well-separated clusters.

The second task is to cluster the main motion of the objects in the dynamic images to let the machine know how they move. The t-distributed stochastic neighbor embedding (t-SNE) was used for feature extraction by reducing 100 high-dimension into 2 low-dimension data, followed by the density-based spatial clustering of applications with noise (DBSCAN) to cluster and gather the similar motion trajectory. The t-SNE can retain the significant structure of the original data and its primary principles are as follows: (1) Stochastic Neighbor Embedding (SNE) is applied to convert high-dimensional Euclidean distances into conditional probabilities representing similarity  $p_{a|b}$ , which indicates the similarity of data  $x_a$  to data  $x_b$  in high-dimensional space<sup>27</sup>; (2)

A "student t-distribution" with one degree of freedom, similar to the Cauchy distribution, is used to obtain the second set of probabilities ( $Q_{alb}$ ) in the low-dimensional space<sup>28</sup>;

(3) Mapping the high-dimensional features  $X$  to low-dimensional features  $Y$  by minimizing the difference cost function ( $\phi$ ) of the sum of Kullback-Leibler divergences, as shown below:

$$\phi = \sum_a \sum_b p_{alb} \log \frac{p_{alb}}{Q_{alb}} \quad (5)$$

For the DBSCAN, it can estimate the density around each point, systematically identifying all core points and expanding each to include all density-reachable points. DBSCAN has the advantage of finding clusters of arbitrary shape and automatically determining the number of clusters  $k$  by optimizing the core parameter 'MinPts' within a neighborhood radius 'r'. After processing all points, those not assigned to a cluster are considered noise points or abnormal points<sup>29</sup>.

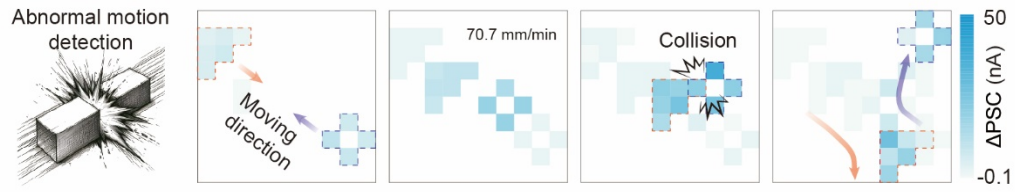
As shown in Figure 5i, the motions recorded by the ideal and denoised images could be correctly clustered. To evaluate the clustering results, the silhouette coefficient value (SCV) ranging from -1 to 1 has been calculated, as shown in Supplementary Fig. 22. The average SCV of the denoised image is 0.695, which is comparable to that of ideal image and is significantly higher than that for noisy image, indicating an enhanced clustering result. The comparison of the clustering accuracy based on the ideal, denoised and noisy images is shown in Supplementary Table 2. The accuracy of the ideal and denoised images is 100% for the 6 types of motion. However, the noisy images demonstrate unreliable results, with incorrect categories, numbers, and ten failed motions for clustering into any category. It means that the complex and advanced algorithms are required to process these noisy images.

**Supplementary Table 2. Comparison of the clustering accuracy.**

<b>Input motion</b>	<b>Motion number</b>	<b>Clustering results</b>		
		<b>Ideal image</b>	<b>Denoised image</b>	<b>Noisy image</b>
Left-center- right	40	40	40	78
Bottom left-center-bottom right	40	40	40	38
Top left-center-top right	40	40	40	39
Bottom right-center-top left	40	40	40	39
Top right-center-bottom left	40	40	40	36
Rotation	40	40	40	*

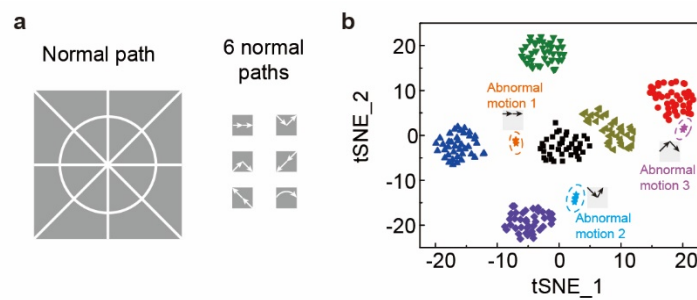
\* means that no motion is classified as rotation. The 10 motions were not classified into any category.

Unsupervised learning methods provide a robust framework for anomaly detection, especially when labeled data is scarce or unavailable. We utilized the array device to record the motion of two objects and the collision process of them (Supplementary Fig. 23). To effectively detect abnormal motion, it is essential to first define what constitutes normal motion. As illustrated in Supplementary Fig. 24a, we have defined the normal paths for object motion. The motion trajectories captured by the bidir-ZC device array along these predefined paths are considered normal. Consequently, motions of the objects that are consistent with the directions in the dataset of Figure 5i are recognized as normal, while any motion not included in the dataset is deemed abnormal (Supplementary Fig. 24a). Obviously, the object deviated the normal path after collision, as shown in Supplementary Fig. 23. To identify these deviations as abnormal motions, we utilized the normal motion dataset along with three additional types of motions recorded by the device, which were then fed into an unsupervised network. As shown in Supplementary Fig. 24b, all the three types abnormal motions could be identified with the correct number of each motion type. The schematic illustrations of the three types motion were also marked next the identified results.



**Supplementary Fig. 23. Collision process recording by the bidir-ZC device array.**

The two objects moved towards each and after the collision, the objects deviated from their original paths to generate these new paths.



**Supplementary Fig. 24. Abnormal motion recognition using the unsupervised learning methods.** **a** Defined normal path of motion. **b** Identified three types of abnormal motions.

## Reference

1. Phillips JC. Stretched exponential relaxation in molecular and electronic glasses. *Rep. Prog. Phys.* **59**, 1133 (1996).
2. Wang Y, *et al.* Negative photoconductance in van der Waals heterostructure-based floating gate phototransistor. *ACS nano* **12**, 9513-9520 (2018).
3. Zhu X, *et al.* Negative Phototransistors with Ultrahigh Sensitivity and Weak-Light Detection Based on 1D/2D Molecular Crystal p-n Heterojunctions and their Application in Light Encoders. *Adv. Mater.* **34**, 2201364 (2022).
4. Hong X, *et al.* Two-Dimensional Perovskite-Gated AlGa<sub>N</sub>/Ga<sub>N</sub> High-Electron-Mobility-Transistor for Neuromorphic Vision Sensor. *Adv. Sci.* **9**, 2202019 (2022).
5. Zhu X, *et al.* High-Contrast Bidirectional Optoelectronic Synapses based on 2D Molecular Crystal Heterojunctions for Motion Detection. *Adv. Mater.* **35**, 2301468 (2023).
6. Chen Y, *et al.* Bidirectional Synaptic Phototransistor Based on Two-Dimensional Ferroelectric Semiconductor for Mixed Color Pattern Recognition. *ACS nano* **17**, 12499-12509 (2023).
7. Fu J, Nie C, Sun F, Li G, Shi H, Wei X. Bionic visual-audio photodetectors with in-sensor perception and preprocessing. *Sci. Adv.* **10**, eadk8199 (2024).
8. Liu C, *et al.* Bipolar synaptic organic/inorganic heterojunction transistor with complementary light modulation and low power consumption for energy-efficient artificial vision systems. *Sci. China Mater.* **67**, 1500-1508 (2024).
9. Pang X, *et al.* Non-volatile rippled-assisted optoelectronic array for all-day motion detection and recognition. *Nat. Commun.* **15**, 1613 (2024).
10. Yang J, *et al.* A Reconfigurable Bipolar Image Sensor for High-Efficiency Dynamic Vision Recognition. *Nano Lett.*, **19**, 5862–5869 (2024).
11. Han J, *et al.* Graphene/organic semiconductor heterojunction phototransistors with broadband and bi-directional photoresponse. *Adv. Mater.* **30**, 1804020 (2018).
12. Hou Y-X, *et al.* Large-scale and flexible optical synapses for neuromorphic

- computing and integrated visible information sensing memory processing. *ACS nano* **15**, 1497-1508 (2020).
13. Dai Q, *et al.* Near-Infrared Phototransistor Based on Graphene/C60/PbPc Heterojunction with Tunable Bidirectional Photoresponse. *Adv. Mater. Interfaces* **9**, 2200116 (2022).
  14. Wen Z, Wang S, Yi F, Zheng D, Yan C, Sun Z. Bidirectional Invisible Photoresponse Implemented in a Traps Matrix-Combination toward Fully Optical Artificial Synapses. *ACS Appl. Mater. Interfaces* **15**, 55916-55924 (2023).
  15. Zhou G, *et al.* Full hardware implementation of neuromorphic visual system based on multimodal optoelectronic resistive memory arrays for versatile image processing. *Nat. Commun.* **14**, 8489 (2023).
  16. Lu C, *et al.* Self-Rectifying All-Optical Modulated Optoelectronic Multistates Memristor Crossbar Array for Neuromorphic Computing. *Nano Lett.*, **5**, 1667–1672 (2024).
  17. Ahmed T, *et al.* Fully light-controlled memory and neuromorphic computation in layered black phosphorus. *Adv. Mater.* **33**, 2004207 (2021).
  18. Gao Z, *et al.* InP Quantum Dots Tailored Oxide Thin Film Phototransistor for Bioinspired Visual Adaptation. *Adv. Funct. Mater.* **33**, 2305959 (2023).
  19. Wu JY, *et al.* Broadband MoS<sub>2</sub> Field-Effect Phototransistors: Ultrasensitive Visible-Light Photoresponse and Negative Infrared Photoresponse. *Adv. Mater.* **30**, 1705880 (2018).
  20. Lian Y, *et al.* Tunable Bi-directional Photoresponse in Hybrid PtSe<sub>2</sub>-x Thin Films Based on Precisely Controllable Selenization Engineering. *Adv. Funct. Mater.* **32**, 2205709 (2022).
  21. Li HK, *et al.* A light-stimulated synaptic transistor with synaptic plasticity and memory functions based on InGaZnO<sub>x</sub>-Al<sub>2</sub>O<sub>3</sub> thin film structure. *J. Appl. Phys.* **119**, 244505 (2016).
  22. John RA, *et al.* Ionotronic halide perovskite drift-diffusive synapses for low-power neuromorphic computation. *Adv. Mater.* **30**, 1805454 (2018).



23. Lei T, Jia X, Zhang Y, Liu S, Meng H, Nandi AK. Superpixel-based fast fuzzy C-means clustering for color image segmentation. *IEEE Trans. Fuzzy Syst.* **27**, 1753-1766 (2018).
24. Askari S. Fuzzy C-Means clustering algorithm for data with unequal cluster sizes and contaminated with noise and outliers: Review and development. *Expert Syst. Appl.* **165**, 113856 (2021).
25. Bezdek JC, Ehrlich R, Full W. FCM: The fuzzy c-means clustering algorithm. *Comput. Geosci.* **10**, 191-203 (1984).
26. Pal NR, Pal K, Keller JM, Bezdek JC. A possibilistic fuzzy c-means clustering algorithm. *IEEE Trans. Fuzzy Syst.* **13**, 517-530 (2005).
27. Van der Maaten L, Hinton G. Visualizing data using t-SNE. *J. Mach. Learn. Res.* **9**, 2579-2605 (2008).
28. Oliveira FHM, Machado ARP, Andrade AO. On the Use of t-Distributed Stochastic Neighbor Embedding for Data Visualization and Classification of Individuals with Parkinson's Disease. *Comput. Math. Methods. Med.* **2018**, 8019232 (2018).
29. Hahsler M, Piekenbrock M, Doran D. dbscan: Fast density-based clustering with R. *J. Stat. Softw.* **91**, 1-30 (2019).